8-1998

Analytic Forms of Bidirectional Reflectance Functions for application to Earth Radiation Budget Studies

N. Manalo-Smith
Old Dominion University

G. L. Smith

S. N. Tiwari

W. F. Staylor

Original Publication Citation

Manalo-Smith, N., Smith, G. L., Tiwari, S. N., & Staylor, W. F. (1998). Analytic forms of bidirectional reflectance functions for application to Earth radiation budget studies. *Journal of Geophysical Research: Atmospheres, 103*(D16), 19733-19751. doi:10.1029/98jd00279

JOURNAL OF GEOPHYSICAL RESEARCH, VOL. 103, NO. D16, PAGES 19,733–19,751, AUGUST 27, 1998

Analytic forms of bidirectional reflectance functions for application to Earth radiation budget studies

N. Manalo-Smith[1,2], G. L. Smith[3,4], S. N. Tiwari[1], and W. F. Staylor[3]

Abstract. Analytic expressions for the bidirectional reflectance functions are formulated and fit to the Earth Radiation Budget Experiment (ERBE) operational models, which were developed using Nimbus 7 ERB data. The analytic bidirectional reflectance distribution functions (BRDFs) are based on theoretical considerations and are functions of viewing geometry and scene type. The models consist of a Rayleigh scattering term and a term for scattering due to clouds and surface. The darkness of the ocean permits the empirical determination of the Rayleigh component of scattering from the atmosphere. The models have the advantage that they are smooth in terms of view and solar zenith angles and relative solar azimuth angle and satisfy reciprocity. Results are presented for the ERBE scene types. The analytic functions closely model the reflectances in the forward scatter direction, but in the backscatter direction, the analytic models are slightly more limb brightened than the ERBE operational models. The model was also fit to the Dlhopolsky/Cess BRDF for clear ocean, which provides a finer angular resolution than the ERBE BRDFs. The results of this study provide a set of BRDFs for ERBE scene types in terms of a set of simple equations and few coefficients for each scene type. These models can be used for mission planning and interpretation of data from future Earth radiation budget missions such as the Clouds and Earth's Radiant Energy System (CERES).

1. Introduction

To enhance our understanding of the radiative energy interaction between Earth and space, the components of the Earth's radiation budget must be examined. The availability of remotely sensed radiance measurements from satellites makes this investigation feasible. The components of the radiation budget are the incident solar flux, the Earth's emitted (longwave) radiation, and the Earth's reflected (shortwave) solar radiation at the top of the atmosphere (TOA), which is considered to be a surface of reference at a specified altitude. The TOA longwave (LW) and shortwave (SW) fluxes are not directly measurable quantities but rather must be derived from the observed radiances. The radiation emerging from the TOA has an anisotropic distribution which is influenced by the reflectance characteristics of the underlying surface, the illumination and viewing conditions, the optical properties of the intervening atmosphere, and the amount of cloud coverage within the scene [*Brennan et al.*, 1965; *Raschke et al.*, 1973; *Larsen and Barkstrom*, 1977; *Smith et al.*, 1986]. The radiance to TOA flux conversion requires knowledge of the angular characteristics of the outgoing radiation field, which is described by angular distribution models or bidirectional reflectance distribution functions (BRDFs), the latter being the term used in this study. Uncertainties in the models lead to errors in the derived fluxes at TOA.

Following earlier investigations of radiation anisotropy [e.g., *Coulson et al.*, 1965; *Salomonson and Marlatt*, 1968; *Ruff et al.*, 1968], the first scanning instruments designed specifically to measure the radiation budget were part of the Earth Radiation Budget (ERB) instrument that flew aboard the Nimbus 6 and 7 satellites [*Smith et al.*, 1977; *Jacobowitz et al.*, 1984] in 1975 and 1978. The BRDF models which were used to process data from the Earth Radiation Budget Experiment (ERBE) [*Barkstrom and Smith*, 1986] were derived from the Nimbus 7 ERB and the Geostationary Operational Environmental Satellite (GOES) data sets by *Suttles et al.* [1988]. *Dlhopolsky and Cess* [1993] utilized ERBE shortwave radiance measurements to generate an improved set of angular directional models with increased angular resolution for clear sky over ocean surface.

The present ERBE operational models are tabulated into ranges of angular coordinates called "bins." Because each bin value is a sample mean, the ERBE models have scatter in each angle bin. There are a large number of angular bins and a limited amount of data on which to base the models, so some angular bins have a small number of measurements. In some angular bins, this scatter results in marked discontinuities from one bin to another. In studies of retrieved flux errors due to scene identification errors, this random scatter dominates the results [*Manalo and Smith*, 1991]. Also, the models do not satisfy the reciprocity principle (i.e., interchanging the incident and reflected directions must yield the same flux contribution). Moreover, there is about a 10% growth in retrieved albedo as the view zenith angle increases from nadir to limb [*Smith et*

[1] Department of Mechanical Engineering, Old Dominion University, Norfolk, Virginia.
[2] Now at Analytical Services and Materials, Inc., Hampton, Virginia.
[3] Formerly at Atmospheric Sciences Division, NASA Langley Research Center, Hampton, Virginia.
[4] Now at Virginia Polytechnic Institute and State University, Hampton, Virginia.

Paper number 98JD00279.
0148-0227/98/98JD-00279$09.00

al., 1988; *Suttles et al.*, 1992]. The accuracy of future radiation budget data products can be enhanced with an improved set of BRDFs. The improved set of BRDFs should be continuous and smooth from one angular bin to another. It should also satisfy reciprocity. Additionally, radiances measured from different viewing angles over a single site must be converted to the same flux if the BRDF is modeled correctly (i.e., there is no change of retrieved albedo with view zenith angle).

The purpose of the present work is to develop BRDF models which satisfy the principle of reciprocity and avoid discontinuities from one discrete angular bin to another as observed in the ERBE operational BRDFs. This study uses two simple analytic formulations of the BRDFs that describe the dependence of the solar reflected radiation on surface, cloud, viewing geometry, and atmospheric conditions for 9 of the 12 ERBE scene types, which are listed in Table 1. The nine basic scene types are classified according to geographical surface type (ocean, land, snow, desert) under varying degrees of cloud cover (clear, partly cloudy, mostly cloudy, overcast). The remaining three scenes are mixed scenes that are assumed to be made up of 50% ocean and 50% land (i.e., coast). The model coefficients are derived by applying an analytic fit to the BRDFs of *Suttles et al.* [1988] which were used to process ERBE data. For each scene type, with the exception of the mixed scenes, a single set of model parameters is required for application to any combination of viewing geometries. Results of this study can be used for mission planning and data interpretation of next generation Earth radiation budget programs such as the Clouds and Earth's Radiant Energy System (CERES) mission [*Barkstrom*, 1990].

The physical problem, including theoretical formulation, is presented in section 2. The analytic forms of the BRDF are developed in section 3. Section 4 covers results and discussion. Finally, conclusions drawn from this study are presented in section 5.

2. Physical Problem and Theoretical Formulation

When solar radiation impinges on the Earth-atmosphere system, it is reflected in various directions. The reflected shortwave radiances are dependent upon the direction from which a surface is being viewed as well as on the surface angular reflectance characteristics. A specular surface, such as a calm ocean surface, behaves much like a mirror and its reflectance is highly directional, while a diffuse surface will reflect uniformly in all directions. In addition to their dependence on the underlying surface, the BRDFs are also influenced by the amount of cloud cover and the state of the intervening atmosphere, for example, amount of aerosols and water vapor.

2.1. Bidirectional Reflectance Model

The target, satellite, and Sun geometry used in this study is depicted in Figure 1 [*Suttles et al.*, 1988]. The angle between the ray to the Sun and the normal to the target area is the solar zenith angle ζ, and the angle between the outgoing ray and the normal to the target area is the viewing zenith angle θ. The relative azimuth angle ϕ is the angular distance of the satellite from the principal plane, i.e. the plane containing the Sun, the Earth's center and the point of observation. The relative azimuth angle for an exiting ray is measured from the principal plane on the side away from the Sun. Thus reflection in the forward direction corresponds to $\phi = 0°$ and backward reflection corresponds to $\phi = 180°$. The reflected shortwave flux M is obtained by integrating the radiances L over all the outgoing directions, so

$$M = \int_0^{2\pi} \int_0^{\pi/2} L(\theta, \phi, \zeta) \cos\theta \sin\theta d\theta d\phi \quad (1)$$

The flux M has units of W m^{-2}, and L has units of W m^{-2} sr^{-1}. For an isotropic surface (i.e., the reflected radiation is the same in all directions), $M = \pi L$. The bidirectional reflectance distribution function (BRDF) R, which characterizes the anisotropy of the reflected radiance, is defined by

$$R(\theta, \phi, \zeta) = \pi L(\theta, \phi, \zeta)/M \quad (2)$$

Values of BRDF equal to unity imply that the assumption of isotropy with a radiance measurement will provide the correct radiant flux.

The normalization condition for R is derived by substituting equation (2) into equation (1), giving

$$\int_0^{2\pi} \int_0^{\pi/2} R \cos\theta \sin\theta d\theta d\phi = \pi \quad (3)$$

Table 1. ERBE[a] Scene Type

Scene Type	Cloud Coverage, %
Clear over ocean	0 to 5
Clear over land	0 to 5
Clear over snow	0 to 5
Clear over desert	0 to 5
Clear over land-ocean mix	0 to 5
Partly cloudy over ocean	5 to 50
Partly cloudy over land-desert	5 to 50
Partly cloudy over land-ocean mix	5 to 50
Mostly cloudy over ocean	50 to 95
Mostly cloudy over land-desert	50 to 95
Mostly cloudy over land-ocean mix	50 to 95
Overcast	95 to 100

[a] ERBE, Earth Radiation Budget Experiment.

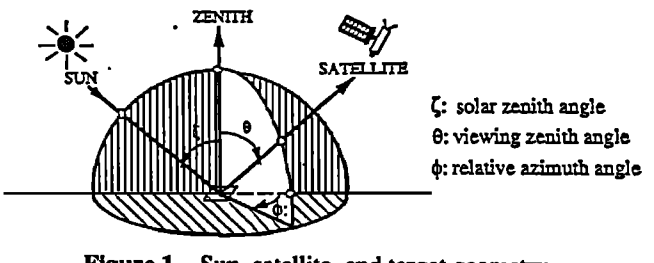

Figure 1. Sun, satellite, and target geometry.

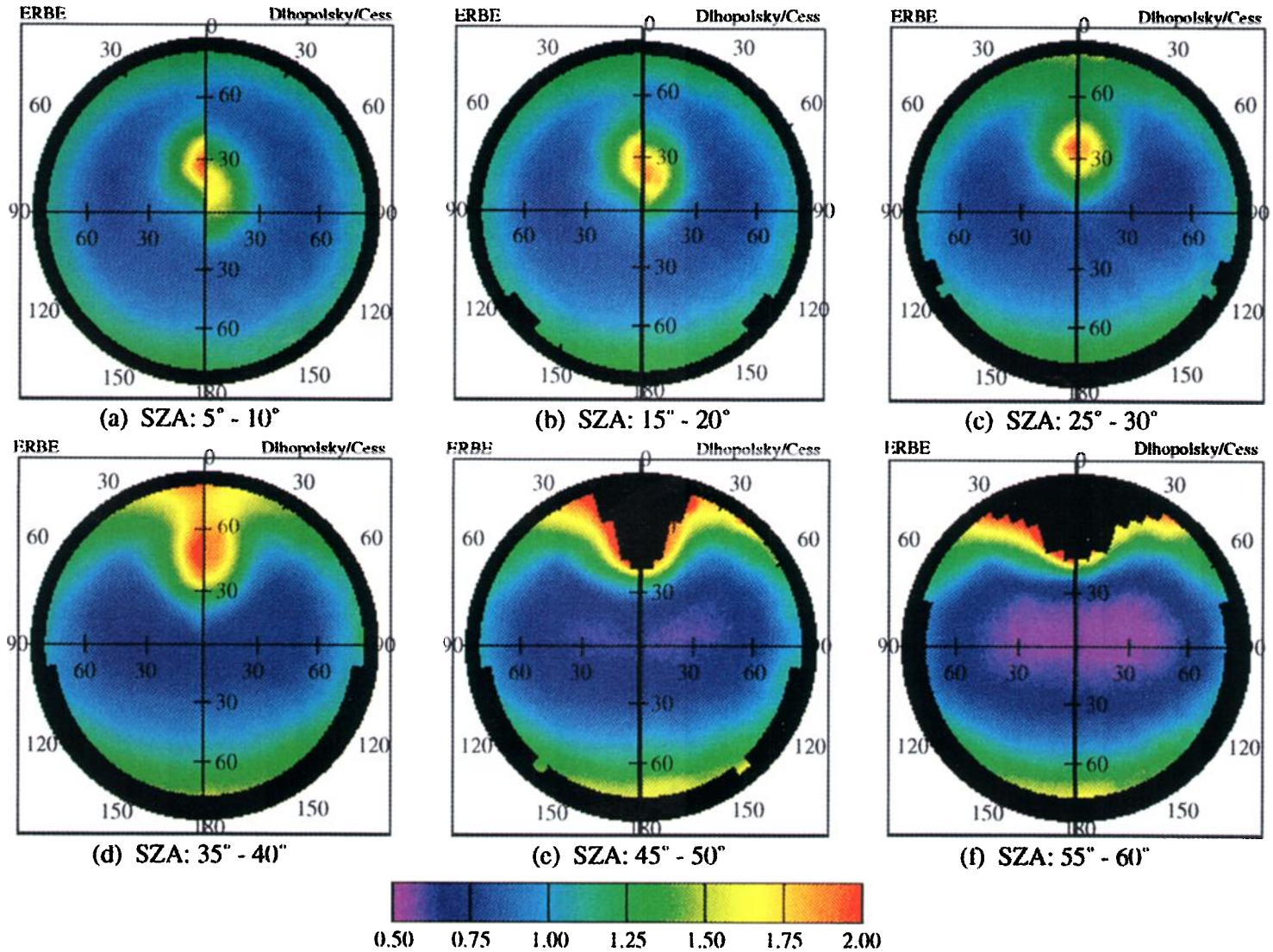

Plate 1. Comparison between Dlhopolsky/Cess and Earth Radiation Budget Experiment (ERBE) Bidirectional Reflectance Distribution Functions (BRDFs).

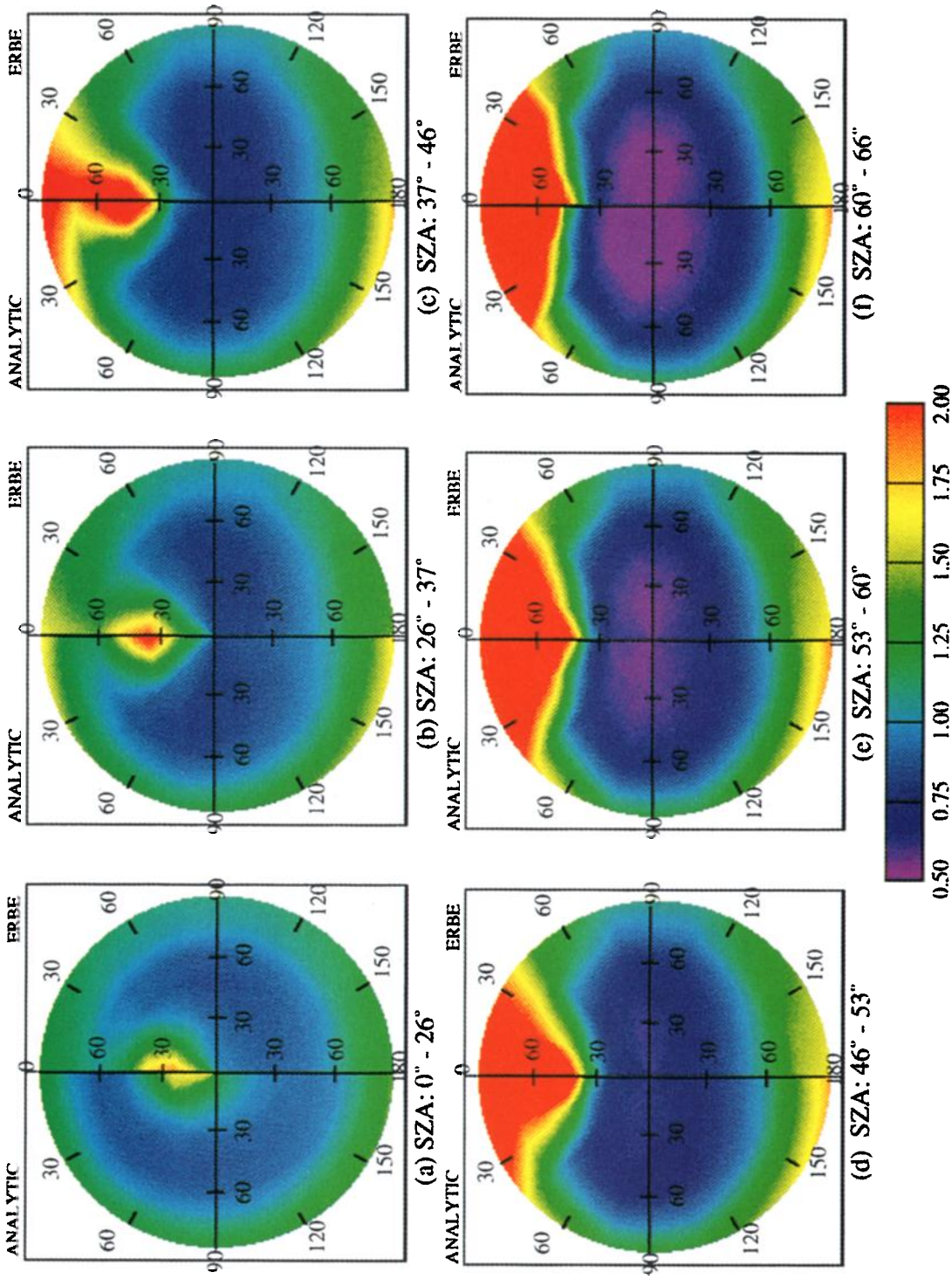

Plate 2. Comparison of analytic and ERBE BRDFs for clear ocean for six solar zenith angle bins.

The albedo a at TOA is defined as

$$a(\zeta) = \frac{M}{S\cos\zeta} \tag{4}$$

where S is the solar flux.

The reflected radiation adheres to the principle of reciprocity [*Chandrasekhar*, 1960], which states that for a given observation point, the positions of the spacecraft and Sun may be interchanged and still yield the same flux contribution. This principle may be expressed as

$$R(\theta, \phi, \zeta)a(\zeta) = R(\zeta, \phi, \theta)a(\theta) \tag{5}$$

The quantity $r(\theta, \phi, \zeta) = R(\theta, \phi, \zeta)a(\zeta)$ is called the bidirectional reflectance.

2.2. BRDFs From Nimbus 7 ERB

The Nimbus 7 ERB broadband scanning radiometer was designed to scan biaxially to gather radiance measurements in all directions for the development of a comprehensive set of BRDFs. However, orbit and scanning constraints inhibited complete angular coverage. *Taylor and Stowe* [1984] constructed BRDFs for eight uniform surface types from ERB data covering a period of 61 days. Results included anisotropic patterns, radiance standard deviations, and relative dispersion within each bin. For their study, these authors determined that only 3% of the bins were not sampled and thus required interpolation. All surfaces studied exhibited an increase in forward scattering with increasing solar zenith angles. The anisotropy patterns of high water and ice clouds are similar, and land surfaces have high backscatter for large solar zenith angles. Water surfaces exhibit limb brightening, and the Sun glint region shifts toward the limb as the Sun moves. Clear snow is limb darkened for $\zeta < 53°$.

Suttles et al. incorporated the *Taylor and Stowe* [1984] results together with GOES narrowband data and theory to generate BRDFs for the 12 scene types listed in Table 1. The surface type is first determined by referring to a static geographical map, while the cloud cover category was identified by a maximum likelihood estimate (MLE) technique [*Wielicki and Green*, 1989]. Table 2 lists the angular bins used by *Suttles et al.* [1988]. The bin sizes were selected as a compromise between the number of samples per bin and the resolution of the BRDFs. The solar zenith angle bins were defined in steps of 0.1 in cosine of solar zenith angle. Sparsely sampled or unsampled angular bins were filled with estimates based on reciprocity, interpolation, or extrapolation.

Dlhopolsky and Cess [1993] used ERBE scanning radiometer data to develop an ocean BRDF with a resolution of 5° x 5° x 5° angular bins. This resolution, permitted by the additional measurements, is a significant refinement compared to the first solar zenith angle bin used by Suttles et al. which covered 0° - 26°. The Dlhopolsky/Cess study determined that the Nimbus 7 angular bin size was not adequate for estimating the anisotropy in this bin range but generally overestimated the instantaneous albedos, especially in the specular directions. Plate 1 compares the ERBE and Dlhopolsky/Cess models for six solar zenith angle ranges. Differences in BRDFs between these models are of the order of 10% for nonspecular directions and increases significantly in the specular direction for solar zenith angles less than 35°. A calculation of the differences between the two models showed that the largest biases occurred for $\zeta > 60°$. The ERBE model is significantly less anisotropic in these solar angles than suggested by the Dlhopolsky/Cess model. Dlhopolsky/Cess also discussed effects of ocean surface roughness on BRDF due to the effects of wind speed. A calm surface reflects a significant amount of energy in the direction of forward scatter. They found that the reflected radiation is higher for a higher wind speed since the wave slope causes the incident angle to be larger.

3. Analytical Bidirectional Reflectance Function

Staylor [1985] and *Staylor and Suttles* [1986] fitted an anisotropic reflectance model to Nimbus 7 measurements of clouds and deserts. The model consists of sum and product terms of the cosines of the solar and viewing zenith angles, thus assuring reciprocity between these angles. This analytic expression has been fit by a nonlinear least squares method to the ERBE operational models tabulated by *Suttles et al.* [1988] to obtain an empirical form for the BRDFs for all cases other than clear

Table 2. ERBE Angular Bin Definition

Bin	Solar Zenith Angle θ_0, deg	Viewing Zenith Angle θ, deg	Relative Azimuth Angle ϕ, deg
1	0 to 25.84	0 to 15	0 to 9
2	25.84 to 36.87	15 to 27	9 to 30
3	36.87 to 45.57	27 to 39	30 to 60
4	45.57 to 53.13	39 to 51	60 to 90
5	53.13 to 60.00	51 to 63	90 to 120
6	60.00 to 66.42	63 to 75	120 to 150
7	66.42 to 72.54	75 to 90	150 to 171
8	72.54 to 78.46		171 to 180
9	78.46 to 84.26		
10	84.26 to 90.00		

ocean and partly cloudy over ocean, which have strong specular reflections. An analytic form of the bidirectional reflectance for clear and partly cloudy over ocean scenes is presented, followed by an analytic model for the other ERBE scene types: land, snow, desert, partly cloudy over land or desert, mostly cloudy over land, desert or ocean, and overcast. The forms of these expressions are based on theoretical considerations.

3.1. Analytic Form of BRDF for Clear and Partly Cloudy Over Ocean

The bidirectional reflectance for clear and partly cloudy over ocean can be expressed in the following empirical form:

$$r_0(\theta, \phi, \zeta) = C_1 + \frac{C_2(1+\cos^2\gamma)}{(uu_0)^{C_3}} + \frac{C_4(C_5-1)}{(uu_0)^{1.5}(C_5-\cos\alpha)^2} \quad (6)$$

where $u = \cos\theta$, $u_0 = \cos\zeta$, γ is the scattering angle, i.e., the angle through which the ray is turned as it is reflected, and α is the angle from the line of specular reflection, i.e., the line in the forward quadrant of the principal plane having the same zenith angle as the incoming ray in the backward quadrant. These angles are given by $\cos\gamma = vv_0\cos\phi - uu_0$ and $\cos\alpha = vv_0\cos\phi + uu_0$, where $v = \sin\theta$ and $v_0 = \sin\zeta$. The first term on the right-hand side is associated with surface albedo and accounts for other diffuse scattering processes. The second term on the right-hand side accounts for Rayleigh scattering from the atmosphere. The Rayleigh phase function is given by $1 + \cos^2\gamma$ and the parameter C_2 is associated with the Rayleigh optical depth. The parameter C_3 accounts for the atmospheric absorption and is affected by the presence of aerosols. This form for atmospheric absorption is used because it is analytically tractable and fits the data well. The last term on the right-hand side accounts for the specular reflection from the ocean surface. When radiation is scattered from a smooth surface, such as the calm ocean, the reflectance distribution is sharply peaked in the forward scatter direction. The form of the specular term was determined by fitting the ERBE operational models choosing an even function in terms of the specular angle α which led to the term $(C_5 - \cos\alpha)^{-2}$.

Because the terms in equation (6) are expressed as sums and/or products of u and u_0, this form satisfies the principle of reciprocity. The expression fits the data best for $uu_0 > 0.1$; however, in order to normalize the expression, it will be used over the full ranges of u and u_0.

The albedo can be computed from equation (6) by integrating it over the upwelling hemisphere (weighted by u). The BRDF integrates to π by the normalization condition, giving

$$a_0(\zeta) = C_1 + C_2 u_0^{-C_3}\left(\frac{3-u_0^2}{2-C_3} + \frac{3u_0^2-1}{4-C_3}\right) + \frac{D}{u_0^2} \quad (7)$$

The last term, which is due to the specular reflection from the ocean surface, is an approximation to the integral, and is independent of C_5. This is because although the radiance is dispersed around the forward scatter peak by an amount depending on C_5, the total contribution to the reflected flux is the same. The computation of D is discussed in the Appendix. The model coefficients for these scene types are listed in Table 3.

Another factor that induces changes in the BRDF is cloud contamination of the scene. ERBE scene identification algorithms classify a scene as clear if the amount of cloud coverage is less than 5%. In order to account for cloud contamination in clear ocean scenes, the bidirectional reflectance is taken to be

$$r(\text{model}) = C_6 r_c + (1-C_6) r_0(\theta, \phi, \zeta) \quad (8)$$

where C_6 is the effective cloud amount within the field of view. The coefficient r_c is the reflectance for cloud, and $r_0(\theta,\phi,\zeta)$ is given by equation (6). C_6 varies from 0 to 5% for clear ocean. The cloud reflectance used is for middle altitude water (MW) clouds, computed by *Staylor* [1985]. The corresponding cloud albedo has been evaluated by *Green and Smith* [1990].

The corresponding albedo for clear ocean is computed as

$$a(\text{model}) = C_6 a_c + (1-C_6) a_0(\zeta) \quad (9)$$

In fitting the analytic model to the ERBE model data tabulated by Suttles et al., data restrictions were imposed. Because of inadequate sampling, Nimbus 7 shortwave data were missing or considered questionable for some angular bins. Therefore for the ERBE models, Suttles et al. used various methods to fill in data for these bins and flagged the filled data for identification. For the analytic model, the flagged bins were not utilized nor were bins for which $uu_0 < 0.1$. Solar zenith angle bins in which the scene type is questionable were also eliminated (e.g., for the Nimbus 7 orbit, $u_0 < 0.3$ might either be ice or snow and not ocean surface). Acceptable data are summarized in Table 4.

Table 3. Model Coefficients for Clear and Partly Cloudy Over Ocean

Scene Type	C_1	C_2	C_3	C_4	C_5	D	RMS
Clear ocean [a]	0.010	0.023	0.800	0.006	1.060	0.011	0.118
Clear ocean [b]	0.005	0.027	0.900	0.008	1.100	0.016	0.110
Partly cloudy over ocean	0.040	0.047	0.577	0.008	1.157	0.016	0.110

[a] Fit to ERBE operational models.

[b] Fit to the Dlhopolsky/Cess models.

Table 4. Constraints Placed on Data Selection

Scene Type	uu_0	u_0	cos γ	cos α
Clear over ocean	>0.1	> 0.3	-1.0 to 1.0	-1.0 to 1.0
Clear over land	>0.1	0.5 to 0.9	-0.95 to 1.0	-1.0 to 1.0
Clear over snow	>0.1	0.1 to 0.6	-1.0 to 1.0	-1.0 to 0.8
Clear over desert	>0.1	0.5 to 1.0	-1.0 to 1.0	-1.0 to 1.0
Partly cloudy over ocean	>0.1	> 0.3	-1.0 to 1.0	-1.0 to 1.0
Partly cloudy over land-desert	>0.1	0.4 to 0.9	-1.0 to 1.0	-1.0 to 1.0
Mostly cloudy over ocean	>0.1	> 0.3	-1.0 to 1.0	-1.0 to 1.0
Mostly cloudy over land-desert	>0.1	0.4 to 0.9	-1.0 to 1.0	-1.0 to 1.0
Overcast	>0.1	0.1 to 1.0	-1.0 to 1.0	-1.0 to 0.9

3.2. Analytic Form of BRDF for Other ERBE Scenes

The bidirectional reflectance for clear land, snow, desert, partly cloudy over land or desert, mostly cloudy over land or desert, mostly cloudy over ocean, and overcast scenes is described by the form used by *Staylor and Suttles* [1986]:

$$r(\text{model}) = \omega r_{\text{Ray}} + \Psi\left[\frac{\Delta r}{\Psi}(\text{model})\right] \tag{10}$$

where r_{Ray} is the bidirectional reflectance due to Rayleigh scattering (second term in equation (6)) and was determined over the ocean. The second term of equation (10) accounts for all other scattering processes. The azimuthal mean reflectance Ψ is defined as

$$\Psi = \frac{1}{\pi}\int_0^{\pi} \Delta r d\phi \tag{11}$$

where $\Delta r = r_{\text{ERBE}} - r_{\text{Ray}}$. The r_{ERBE} is computed from the tabulation of Suttles et al. The azimuthal mean reflectance Ψ and the bracketed expression $\left[\frac{\Delta r}{\Psi}(\text{model})\right]$ are each expressed by regressions.

For scenes with cloud cover, Rayleigh scattering is reduced due to the decreased amount of atmosphere above the reflecting surface. For a scene considered overcast (i.e. cloud amount > 95%), the mean cloud tops are assumed to be at 680 mbar, thus two thirds of the Rayleigh model, as determined over the ocean, is used. As the cloud amount decreases, the amount of Rayleigh scattering increases. The weighting factor ω describes the reduction in Rayleigh-scattering effects due to increased cloudiness.

The azimuthal mean reflectance Ψ can be expressed in terms of the viewing zenith and azimuth angles by [*Staylor*, 1985]:

$$Y = A + BX^2 \tag{12}$$

where $Y = \Psi uu_0$ and $X = (uu_0)/(u + u_0)$. *Staylor* [1985] discusses the significance of the A and B regression coefficients. The last term of equation (10) is computed from the following expression [*Staylor and Suttles*, 1986]:

$$\frac{\Delta r}{\Psi}(\text{model}) = \frac{1 + K(G + \cos\gamma)^2}{1 + K\left[G^2 - 2Guu_0 + (uu_0)^2 + \frac{1}{2}(vv_0)^2\right]} \tag{13}$$

where G and K are fit to the data.

As in the clear and partly cloudy over ocean cases, restrictions on the ERBE models were imposed to exclude questionable scene types, angular bins that have little or no sampling, and angular bins whose BRDFs were calculated using any one of the interpolation techniques discussed above. The model coefficients for these scene types, as well as the Rayleigh weighting factors, are tabulated in Table 5.

The model albedo a (model) is computed using the relation

$$a(\text{model}) = \omega a_{\text{Ray}} + \Delta a \tag{14}$$

where the albedo contribution of Rayleigh scattering is the second term in equation (7) and Δa is expressed as

$$\Delta a = 2\frac{A}{u_0} + 2Bu_0\left[1 + u_0 - 2u_0 ln(1 + u_0) + 2u_0 lnu_0 - \frac{u_0^2}{1 + u_0}\right] \tag{15}$$

The BRDF is then computed by dividing the bidirectional reflectance by the albedo.

4. Results and Discussion

The BRDFs for the clear and partly cloudy over ocean cases are described by equation (6) and are discussed first. The dark ocean permits a good determination of the Rayleigh-scattering term, which is then used for the other seven models. Next, the remaining cases, which are described by equation (10), are discussed.

The ERBE models are determined by averaging data over a grid cell. Because it is nonlinear, the average value of the analytic model is not the value at the center. In order to compare the analytic models to the ERBE models, the average value was computed using 200 realizations which were uniformly distributed over solar zenith, viewing zenith, and relative azimuth. Instrument noise of the order of 1-2 W m^{-2} sr^{-1} was included in the radiance calculations. Similarly, the ERBE models that are plotted correspond to the bin mean values determined by trilinearly interpolating over the given illumination and viewing angles as is done by the ERBE data processing system.

The patterns of bidirectional reflectance functions are presented on polar contour diagrams. The radial coordinate corre-

Table 5. Model Coefficients for Selected Scene Types

Scene Type	A	B	G	K	Rayleigh Weight Factor	RMS
Clear land	0.002	0.384	0.138	0.650	1.000	0.006
Clear Snow	0.011	2.517	0.675	0.188	1.000	0.012
Clear desert (all)	-0.003	0.784	0.025	0.412	1.000	0.015
Clear desert (Sahara)	0.008	0.967	0.138	0.338	1.000	0.019
Partly cloudy over land-desert	0.009	0.643	0.350	0.900	0.917	0.015
Mostly cloudy over ocean	0.024	0.812	0.525	0.988	0.758	0.124
Mostly cloudy over land-desert	0.030	1.019	0.463	0.988	0.758	0.036
Overcast	0.024	1.530	0.500	0.625	0.667	0.028

sponds to the satellite zenith angle θ, while the angular coordinate represents the relative azimuth angle ϕ between the satellite and the Sun (Figure 1). It is assumed that the reflection pattern is symmetric about the principal plane, thus only ϕ = 0°-180° is shown. Although restrictions were imposed on the ERBE tabulated models to remove questionable data, the BRDF is computed here for all combinations of viewing and incident angles. For the BRDF plots, presented in section 4.1, the left portion of a contour polar diagram represents the analytical BRDF, while the right portion represents the ERBE or Dlhopolsky/Cess mean BRDF.

4.1. ERBE Clear Ocean Model

The C_i coefficients for fitting equation (6) to the clear ocean ERBE model are given in Table 3. The root-mean-square (RMS) of the bidirectional reflectance differences between the *Suttles et al.* [1988] data and the model is also listed.

The values in Table 3 are based on mean radiances and thus describe the mean model. However, the C_i coefficients will vary because of the variations that exist in the atmosphere and the underlying surface. With high winds the waves over the ocean will cause the forward scattering peak to broaden (increasing C_5), while for calm conditions, the ocean surface will be flat, thus causing the reflection to be sharply peaked (decreasing C_5) [*Cox and Munk*, 1954]. The diffuse part of radiation which is described by C_1 varies, depending upon the sea state, particles in suspension in the water, and atmospheric turbidity. Variability of water vapor in the atmosphere affects the Rayleigh-scattering term and the absorption of radiation which causes C_3 to vary.

Figure 2 shows the variation of the specular term with cos α for the clear ocean model of Suttles et al. The form used for the third term of equation (6) was found to fit the data well. Plate 2 compares the mean BRDF for clear ocean for the analytic model with the Suttles et al. tabulation for six solar zenith angle bins. For solar zenith angle range 0° - 26° and ϕ = 0°, the largest BRDF occurs in the θ = 15°- 27° range for ERBE, while the analytical BRDF is a maximum in the area of θ = 10°. At small viewing zenith angles (θ < 30°), BRDF decreases as the ζ increases. For large θ, however, BRDF increases significantly with increasing solar zenith angles. All ζ ranges exhibit an increase in anisotropy toward the limb (limb brightening). This is attributed to atmospheric scatter toward the limb over a dark ocean surface. Forward scattering is more prominent than backward scattering. The BRDF variation for ϕ = 90° is more isotropic. The analytic expression provides a good fit to the ERBE BRDF.

4.2. Dlhopolsky/Cess Clear Ocean Model

The analytic model coefficients were also fit to the Dlhopolsky/Cess BRDF data set and are listed in Table 3. Plate 3 compares the BRDF for the analytic model and the Dlhopolsky/Cess model for the angular bins for which Dlhopolsky/Cess had adequate sampling. Unlike the ERBE model for ζ < 25°, the Sun angle for peak specular reflection for the analytic model agrees reasonably well with that of the Dlhopolsky/Cess model. The Dlhopolsky/Cess model is more anisotropic in this region. Both exhibit limb brightening at higher solar angles although the analytic model is more anisotropic in this region. Near zenith, both models are in good agreement.

4.3. Partly Cloudy Over Ocean

For this case, the specular peak is prominent and equation (6) provides a better description of partly cloudy over ocean

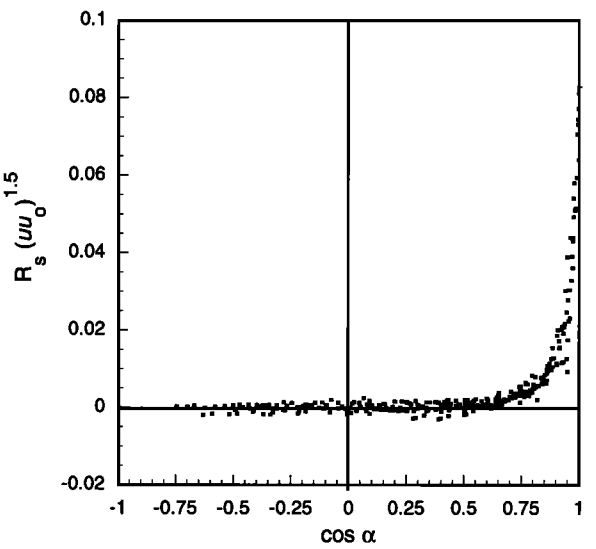

Figure 2. Specular term $R_s(uu_0)^{1.5}$ as a function of cos α.

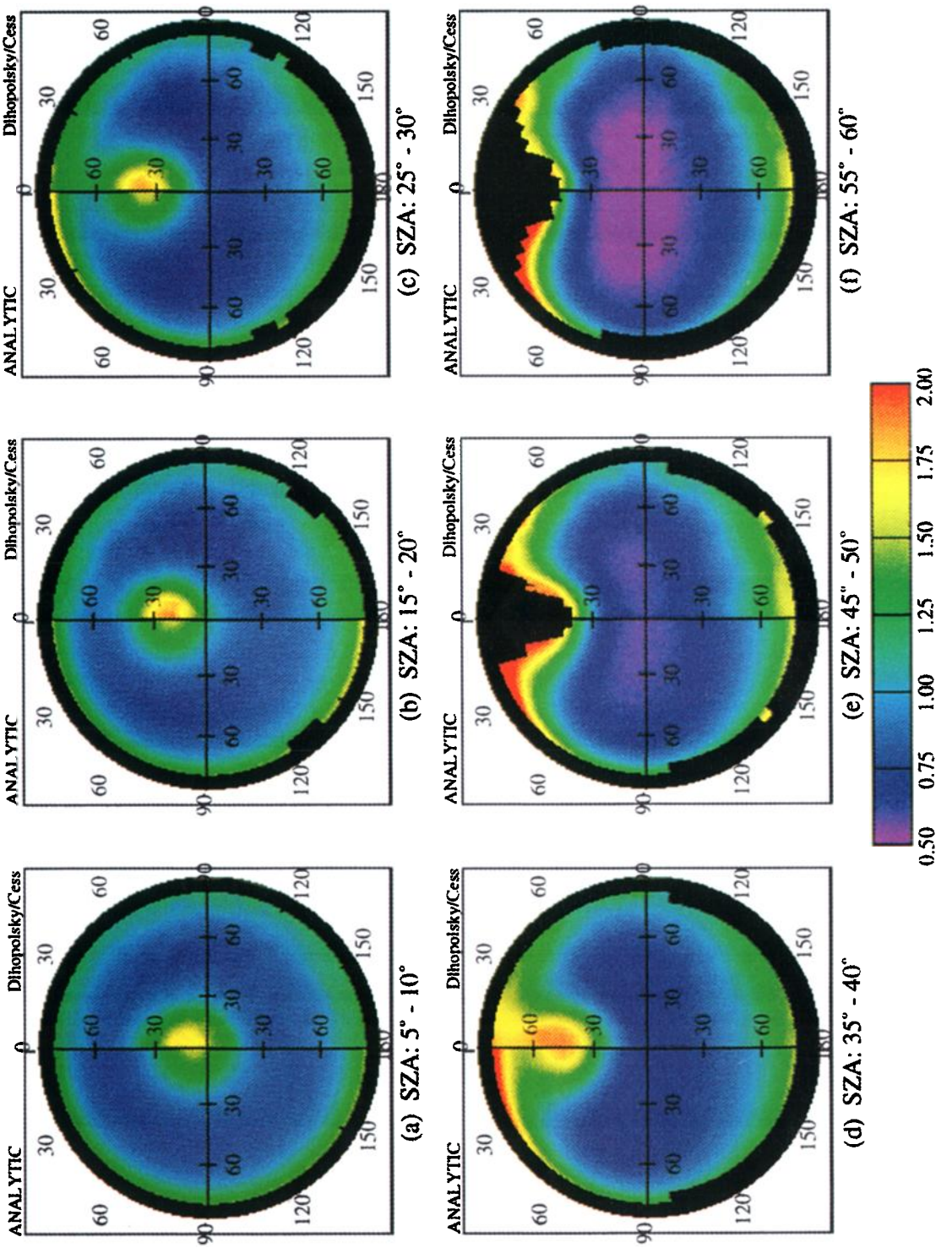

Plate 3. Comparison of analytic and Dihopolsky/Cess BRDFs for clear ocean for six solar zenith angle bins.

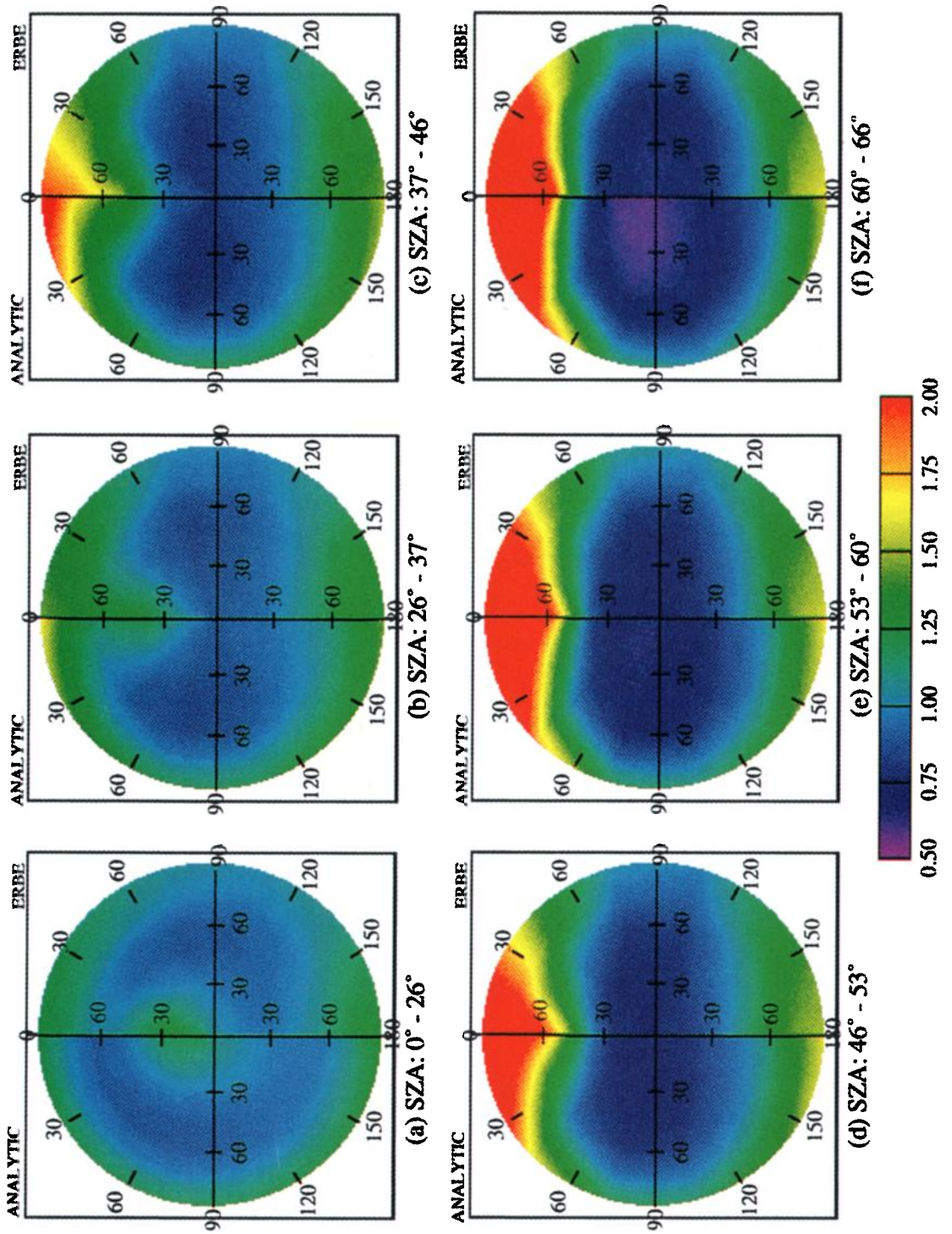

Plate 4. Comparison of analytic and ERBE BRDFs for partly cloudy over ocean for six solar zenith angle bins.

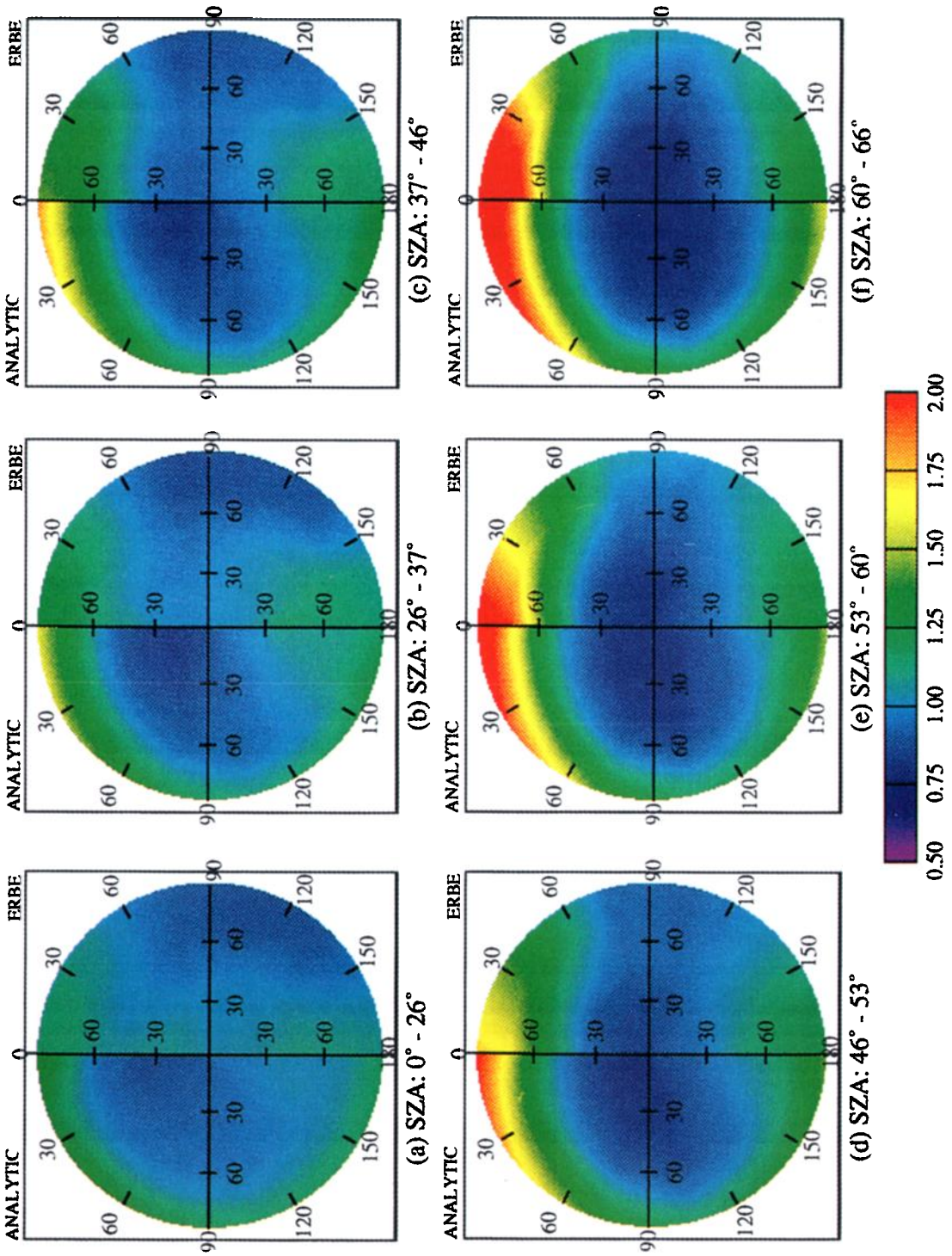

Plate 5. Comparison of ERBE and analytic BRDF for mostly cloudy over ocean.

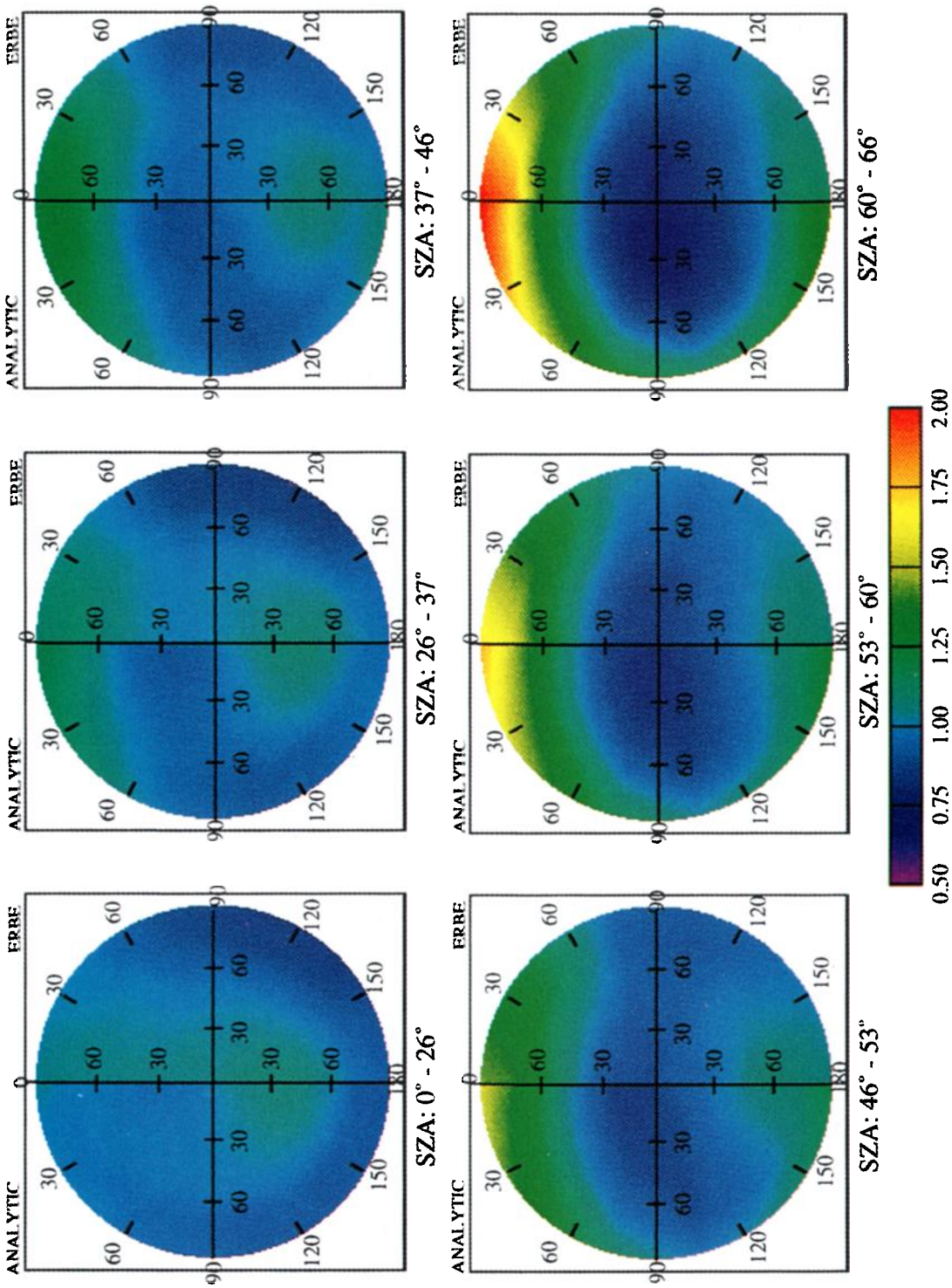

Plate 6. Comparison of Analytic and ERBE BRDFs for overcast for six solar zenith angle bins.

than equation (10). The model coefficients are tabulated in Table 3. Plate 4 compares the analytical and ERBE BRDFs. The peak of specular reflection is evident and shifts toward the horizon as the solar zenith angle increases. Limb brightening in the forward scatter direction is very prominent and broad. The BRDF variation for $\phi = 90°$ is more isotropic.

4.4. Models for Other Scenes

For the remaining seven models, including mostly cloudy over ocean, the specular peak does not appear, and equation (10) fits the data better than equation (6). For each cloud/surface condition, the weighting factor ω for the Rayleigh reflectance term is specified on the basis of mean height of the radiating surface. The coefficients A and B are computed using equation (13) by regression of the directional parameter $Y = \Psi u u_0$ with $X = (u u_0)/(u + u_0)$. Finally, the G and K coefficients for the azimuthal dependence are computed by a least squares fit of equation (13) to $\Delta r/\Psi$ as computed from Suttles et al. These coefficients and the RMS difference between the measured and the computed reflectances are listed in Table 5 for the eight scene types.

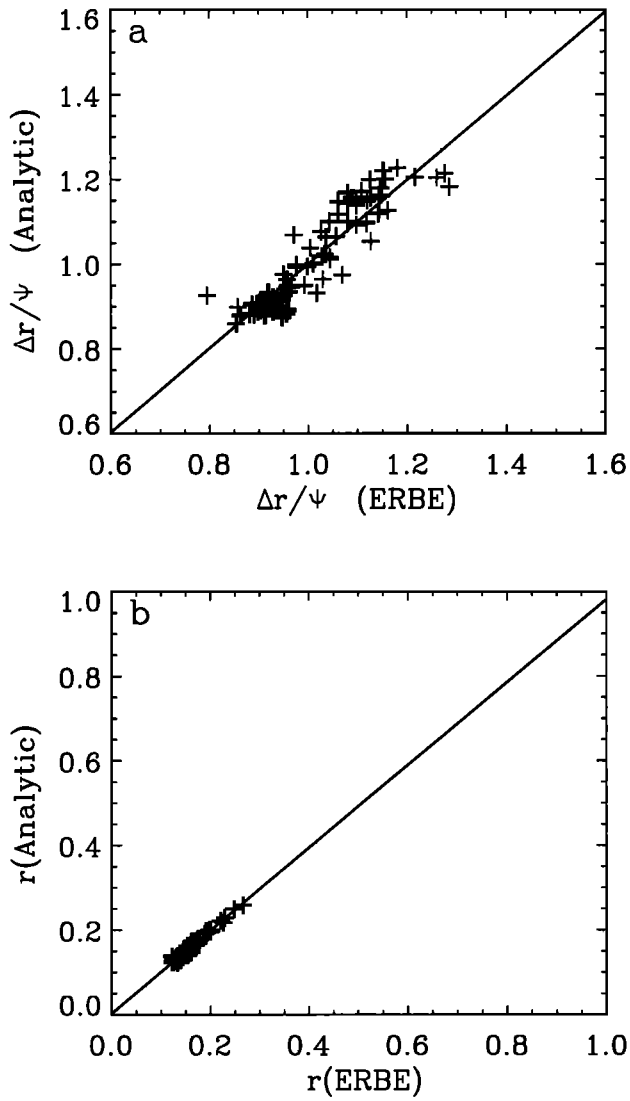

Figure 3. Comparison of analytic model with ERBE model for clear land. (a) Comparison of $\Delta r/\Psi$(analytic) with $\Delta r/\Psi$(ERBE). (b) Comparison of analytic and ERBE bidirectional reflectance.

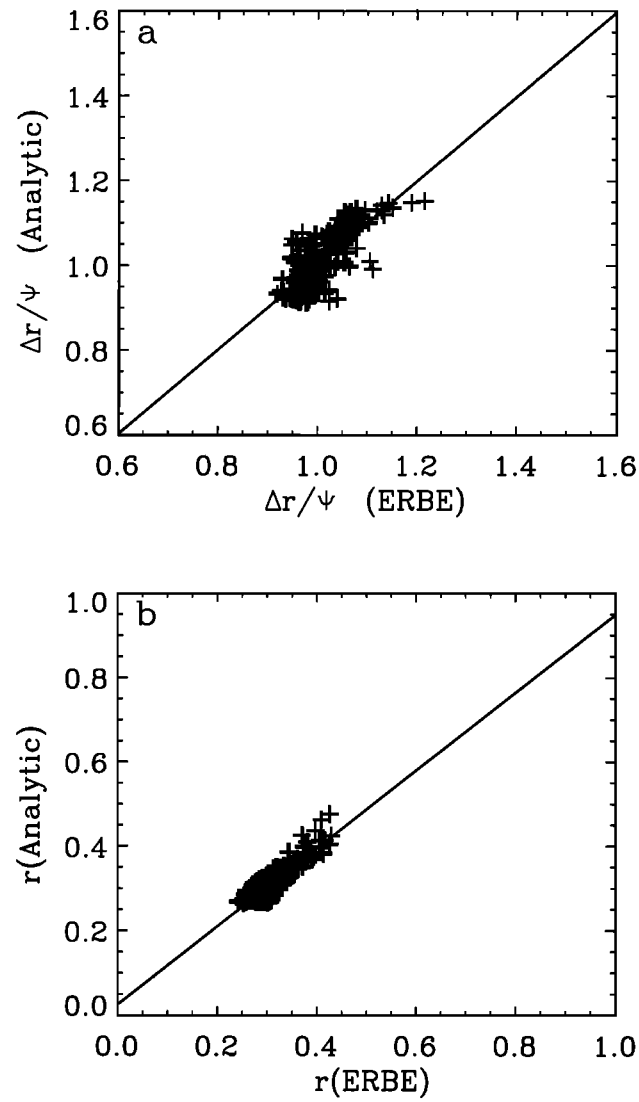

Figure 4. Comparison of analytic model with ERBE model for clear Sahara Desert. (a) Comparison of $\Delta r/\Psi$(analytic) with $\Delta r/\Psi$(ERBE). (b) Comparison of analytic and ERBE bidirectional reflectance.

For clear land, Figure 3a shows the fit of equation (13) to $\Delta r/\Psi$ for data from Suttles et al. The altitude of most land is low enough that the Rayleigh term is not reduced and $\omega = 1$. Figure 3b compares the bidirectional reflectances of the analytic model and the ERBE model. The agreement is better for the bidirectional reflectance r than for the directional parameter $\Delta r/\Psi$, which accentuates differences. The bidirectional reflectances are well correlated, with RMS = 0.006.

For this study, the Sahara Desert is taken as one case, and the combination of all deserts, as listed by Suttles et al., is taken as another, as was done by *Staylor and Suttles* [1986]. Figure 4a shows that for the Sahara the $\Delta r/\Psi$ (analytic) and the $\Delta r/\Psi$ (ERBE) are not well correlated, having a regression factor of 0.599. However, Figure 4b shows that the Sahara bidirectional reflectances are better correlated with an RMS of 0.019. The regression coefficient is small for the Sahara case

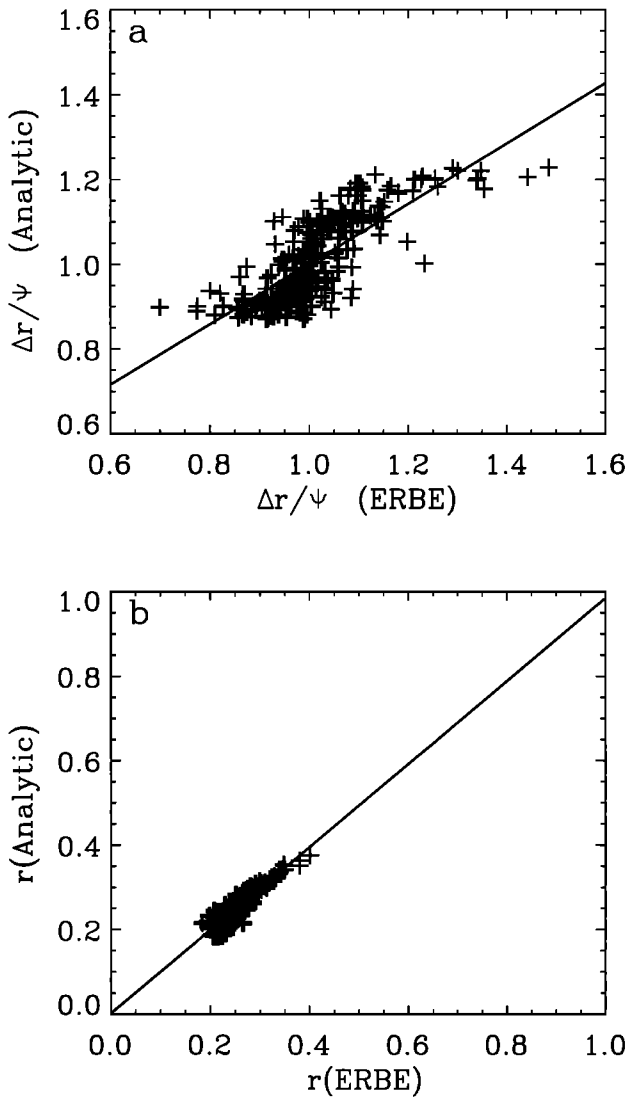

Figure 5. Comparison of analytic model with ERBE model for (all) clear deserts. (a) Comparison of $\Delta r/\Psi$(analytic) with $\Delta r/\Psi$(ERBE). (b) Comparison of analytic and ERBE bidirectional reflectance.

because orbital constraints of the Nimbus 7 spacecraft limit the solar zenith angles to a small range for the Sahara Desert, but for the all-deserts case the range of solar zenith angles is greater. Figure 5 compares the bidirectional reflectances of Suttles et al. to the analytic model for the all-deserts case. Again, although the $\Delta r/\Psi$ are not well correlated, the model and tabulated reflectances are well correlated.

The clear snow reflectances are shown in Figure 6, which shows that the $\Delta r/\Psi$ and bidirectional reflectances are fairly well correlated.

Because of sparsity of data, Suttles et al. combined partly cloudy over land and over desert into one scene type and mostly cloudy over land and over desert into one. The partly cloudy over land-desert reflectance parameters are shown in Figure 7, and mostly cloudy over land-desert reflectance parameters are depicted in Figure 8.

Figure 9 depicts the variation of the directional reflectance Y with the zenith angles parameter X for mostly cloudy over ocean. The regression coefficient is very close to 1.0, indicating that the use of these parameters to describe the BRDF for mostly cloudy over ocean is suitable. Plate 5 compares the ERBE and analytic BRDF. For $\zeta < 37°$, both models are nearly isotropic. For ζ between 37° and 46°, limb brightening is more prominent for the analytic than for the ERBE functions. Both models exhibit limb brightening for $\zeta > 53°$, and the forward scattering peak is more pronounced.

For overcast scenes the Rayleigh weighting factor is two thirds of the clear ocean Rayleigh model, based on the assumption that the mean cloud tops are at 680 mbar. Figure 10 shows the directional reflectance parameter Y as a function of X. Figure 11a shows the comparison of model $\Delta r/\Psi$ with $\Delta r/\Psi$ from ERBE overcast, and Figure 11b compares the analytic and ERBE model bidirectional reflectances. For this study, there was no attempt to discriminate the overcast models by cloud optical thickness, cloud height, or cloud liquid water content, as was done by *Staylor* [1986]. Nevertheless, a comparison with his results shows that the overcast model falls into the

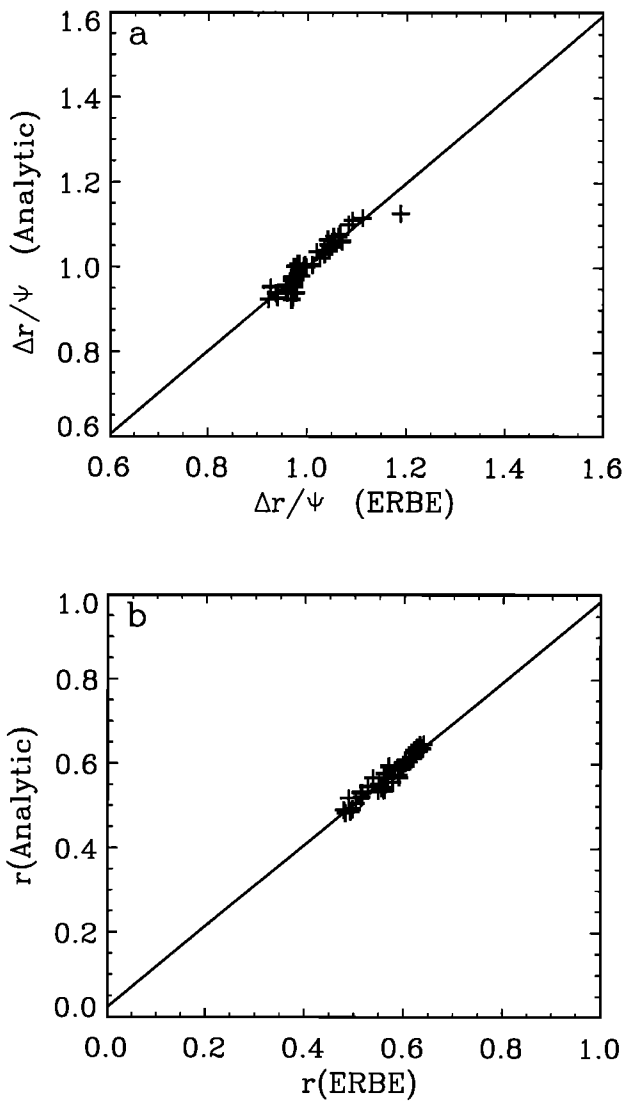

Figure 6. Comparison of analytic model with ERBE model for snow. (a) Comparison of $\Delta r/\Psi$(analytic) with $\Delta r/\Psi$(ERBE). (b) Comparison of analytic and ERBE bidirectional reflectance.

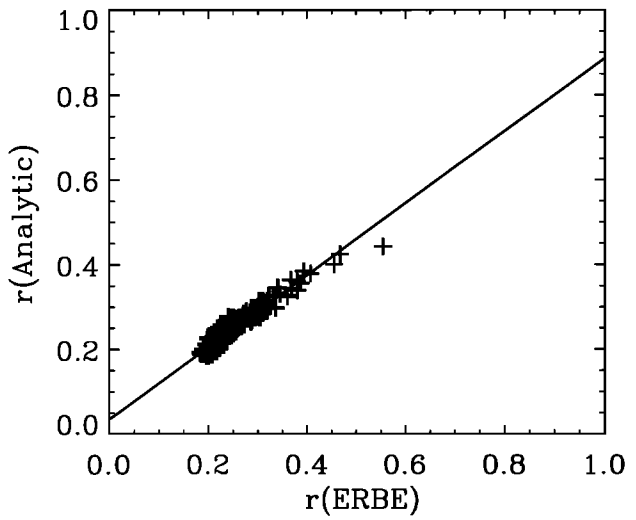

Figure 7. Comparison of analytic and ERBE bidirectional reflectance for partly cloudy over land/desert.

"low-water" category. The scatter diagram shows a strong forward scatter peak, minimum BRDF at $90° < \gamma < 120°$, and a leveling off to a BRDF value of 1.0 at the scattering angles greater than 120°.

The mean BRDFs are illustrated in Plate 6 for $\zeta < 66°$. For $\zeta < 37°$, clouds are limb darkened in the backscatter direction, while for $37° < \zeta < 46°$, clouds are almost isotropic with $\theta < 60°$. At higher ζ, clouds become more anisotropic, and limb brightening, especially in the forward scatter region, becomes more discernible.

4.5. Albedos

The analytic model albedos computed from equation (15) are plotted in Figure 12 as a function of solar zenith angle for $u_0 > 0.1$. All scenes exhibit an increase of model albedo with increasing solar zenith angle, except for clear snow. Clear land is not a highly reflective surface due to the presence of vegetation. Clear desert is a brighter surface since it is generally composed of light sand and little or no vegetation. As the cloud cover increases over land, the corresponding albedo increases. The cloudy scenes over land have albedos that are distributed between the clear land and the overcast scenes, while the snow scene has the highest albedo. These model albedos are in good agreement with those determined for the ERBE operational directional models.

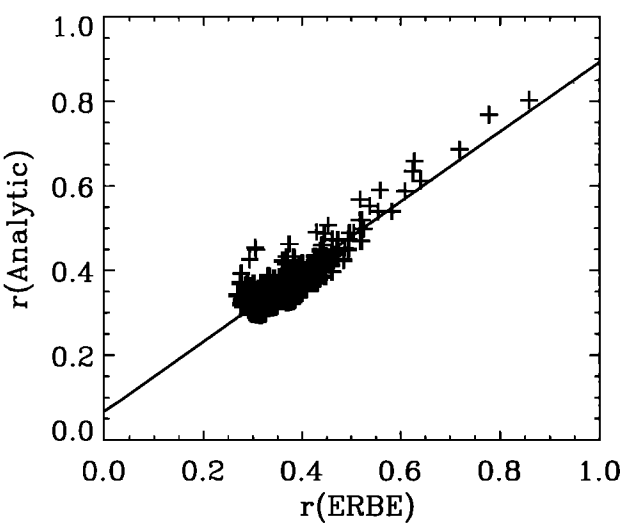

Figure 8. Comparison of analytic and ERBE bidirectional reflectance for mostly cloudy over land/desert.

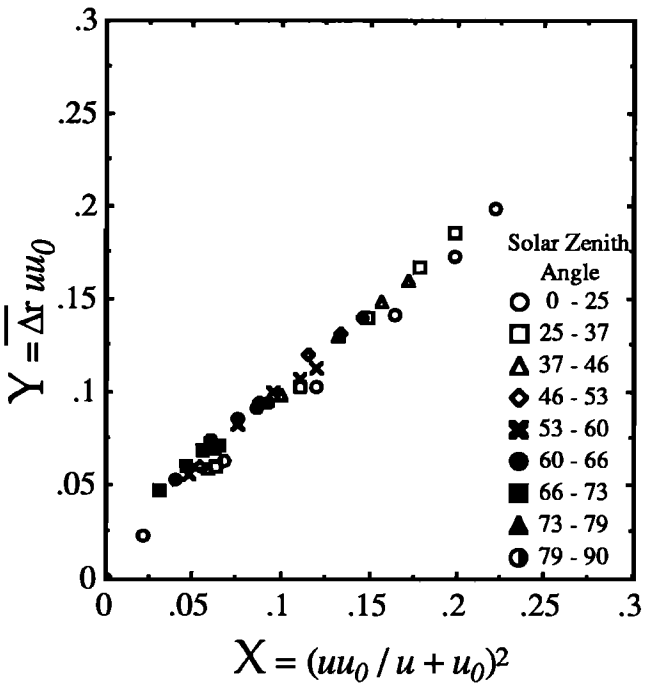

Figure 9. Variation of directional reflectance with directional angles for mostly cloudy over ocean.

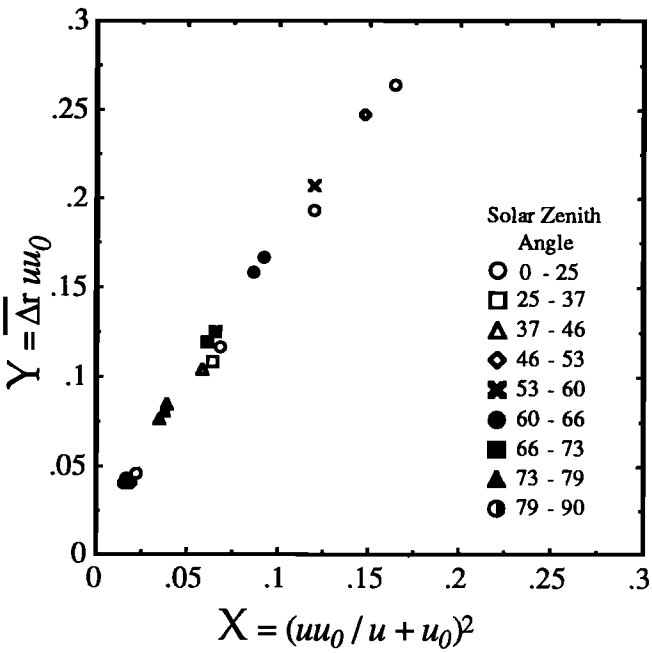

Figure 10. Variation of directional reflectance with directional angles for overcast.

5. Conclusions

Analytic expressions for the bidirectional reflectance functions are formulated and fit to the ERBE operational models, which were developed by Suttles et al. The analytic BRDFs are based on functional forms suggested by theoretical and empirical considerations and vary with viewing geometry and scene type. The models consist of a Rayleigh scattering term and a term for scattering due to clouds and surface. The darkness of the ocean permits the empirical determination of the Rayleigh component of scattering from the atmosphere. The models have the advantage that they are smooth in terms of view and solar zenith angles and relative solar azimuth angle and satisfy reciprocity. Thus these models are free of the marked discontinuities from one angle bin to another. In studies of retrieved flux errors due to scene identification errors, the random scatter dominates the results. Results are presented for the ERBE scene types. The analytic functions closely model the reflectances in the forward scatter direction, but in the backscatter direction, the analytic models are slightly more limb brightened than the ERBE operational models.

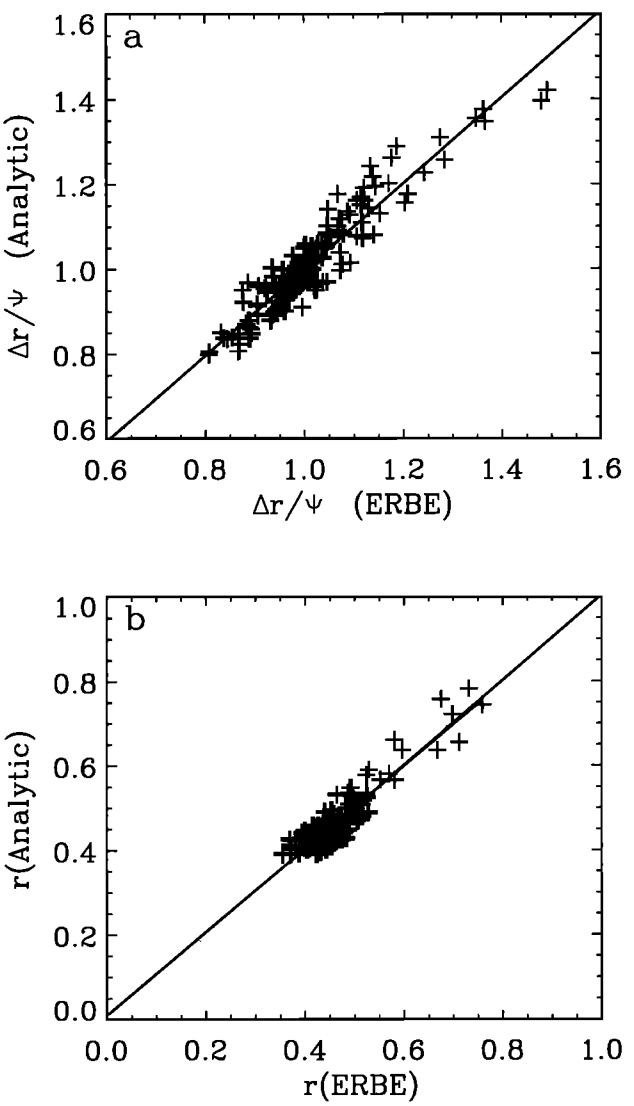

Figure 11. Comparison of analytic model with ERBE model for overcast. (a) Comparison of Δr/Ψ(analytic) with Δr/Ψ(ERBE) for overcast. (b) Comparison of analytic and ERBE bidirectional reflectance.

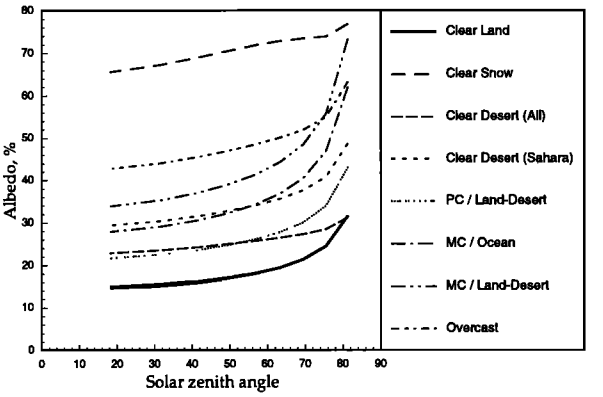

Figure 12. The analytic model albedos as a function of solar zenith angle for each of the scene types.

The model was also fit to the Dlhopolsky/Cess BRDF for clear ocean, which provides a finer angular resolution than the ERBE BRDFs. The results of this study provide a set of BRDFs for all ERBE scene types in terms of a set of simple equations and few coefficients for each scene type. These models can be used for mission planning and interpretation of data from future Earth radiation budget missions such as CERES.

Appendix: Approximation of Specular Albedo for Clear and Partly Cloudy Over Ocean

The specular reflectance is expressed as

$$r_s(\theta, \phi, \varsigma) = \frac{C_4(C_5 - 1)}{(uu_0)^{1.5}(C_5 - \cos\alpha)^2} \tag{A1}$$

where $u = \cos\theta$, $u_0 = \cos\zeta$, and α is the angle from the line of specular reflection given by $\cos\alpha = vv_0\cos\phi + uu_0$, where $v = \sin\theta$ and $v_0 = \sin\zeta$. The directional reflectance R_s is obtained by eliminating the azimuthal dependence. R_s is defined as

$$R_s = \frac{1}{\pi}\int_0^{\pi} r_s d\phi \tag{A2}$$

Substituting equation (A1) into equation (A2) gives

$$R_s = \frac{1}{\pi}A_1 A_2 \tag{A3}$$

where $A_1 = \dfrac{C_4(C_5 - 1)}{(uu_0)^{1.5}}$ $\quad A_2 = \displaystyle\int_0^{\pi} \frac{d\phi}{(C_5 - \cos\alpha)^2}$.

Since A_2 is of the form

$$\int \frac{dx}{(m + n\cos x)^2} \tag{A4}$$

where $m = C_5 - uu_0$ and $n = -vv_0$,

$$A_2 = \frac{m\pi}{(m^2 - n^2)^{1.5}} \tag{A5}$$

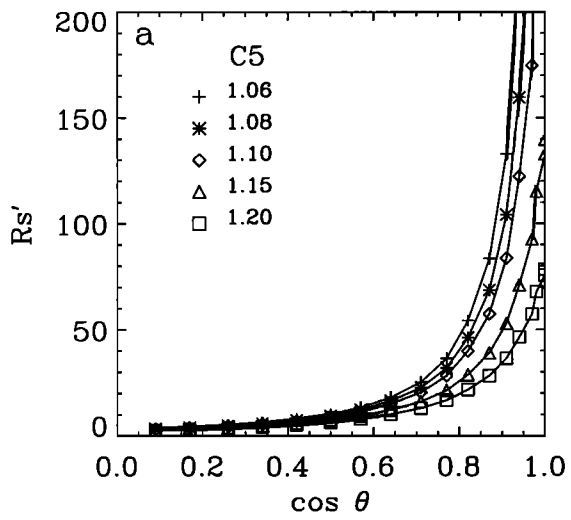

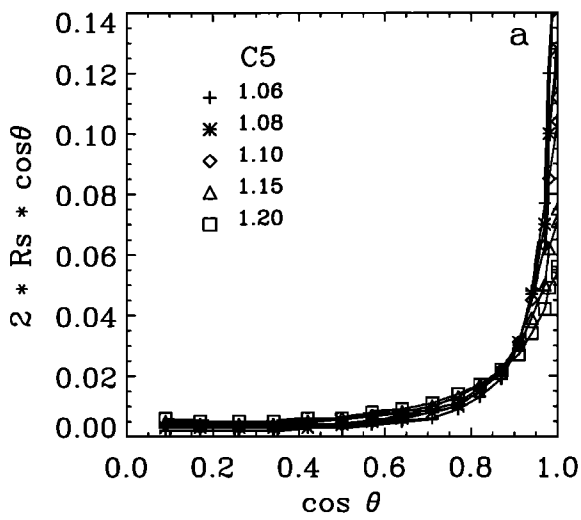

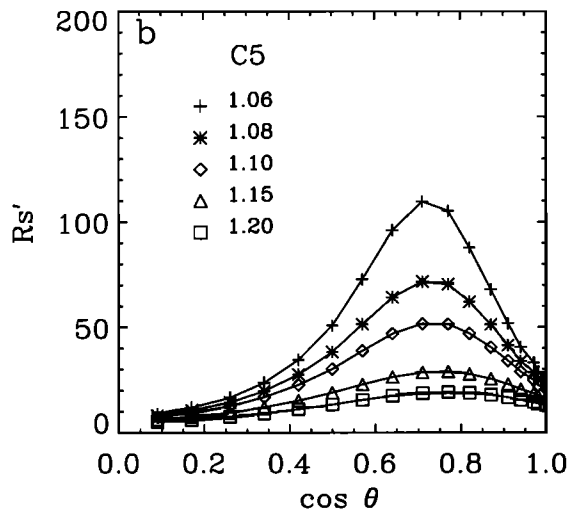

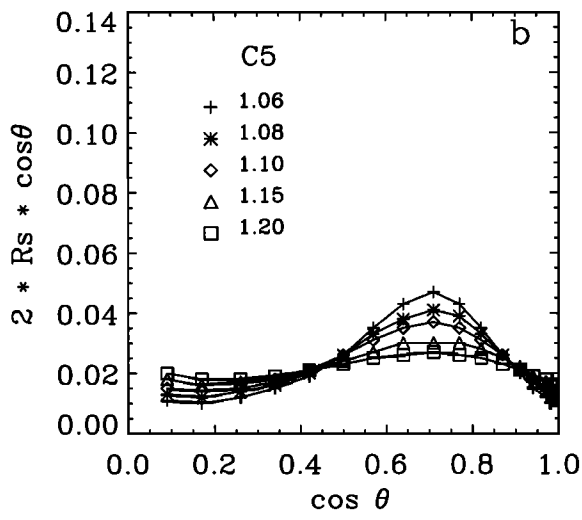

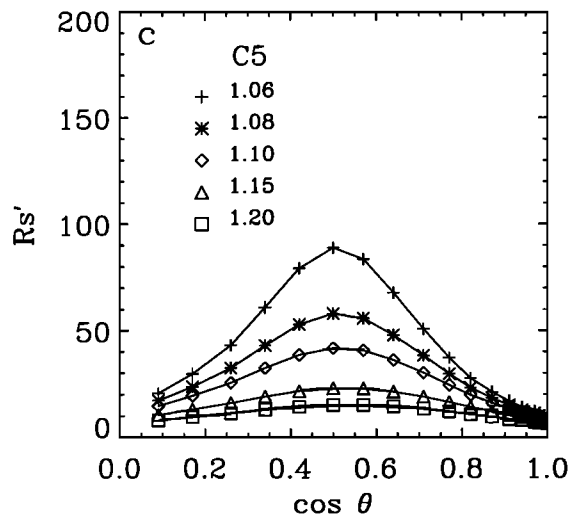

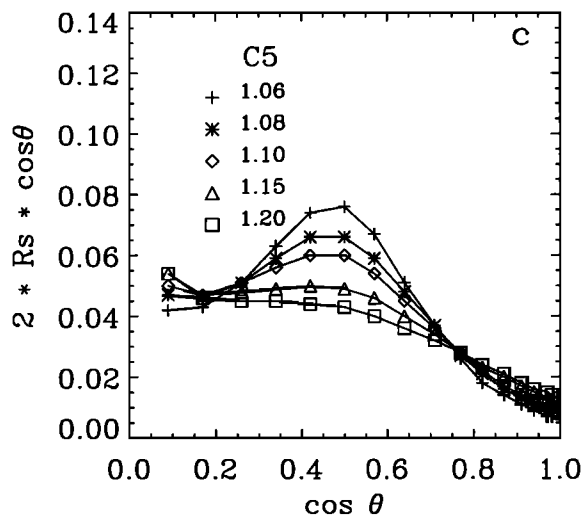

Figure A1. Specular term $A_2 = \int_0^{\pi} \frac{d\phi}{(C_5 - \cos\alpha)^2}$ vs. $\cos\alpha$. (a) SZA = 0°; (b) = SZA = 45°; (c) SZA = 60°.

Figure A2. Specular term $2R_s\cos\theta$ vs. $\cos\alpha$ for $C_4 = 0.0056$. (a) SZA = 0°; (b) = SZA = 45°; (c) SZA = 60°.

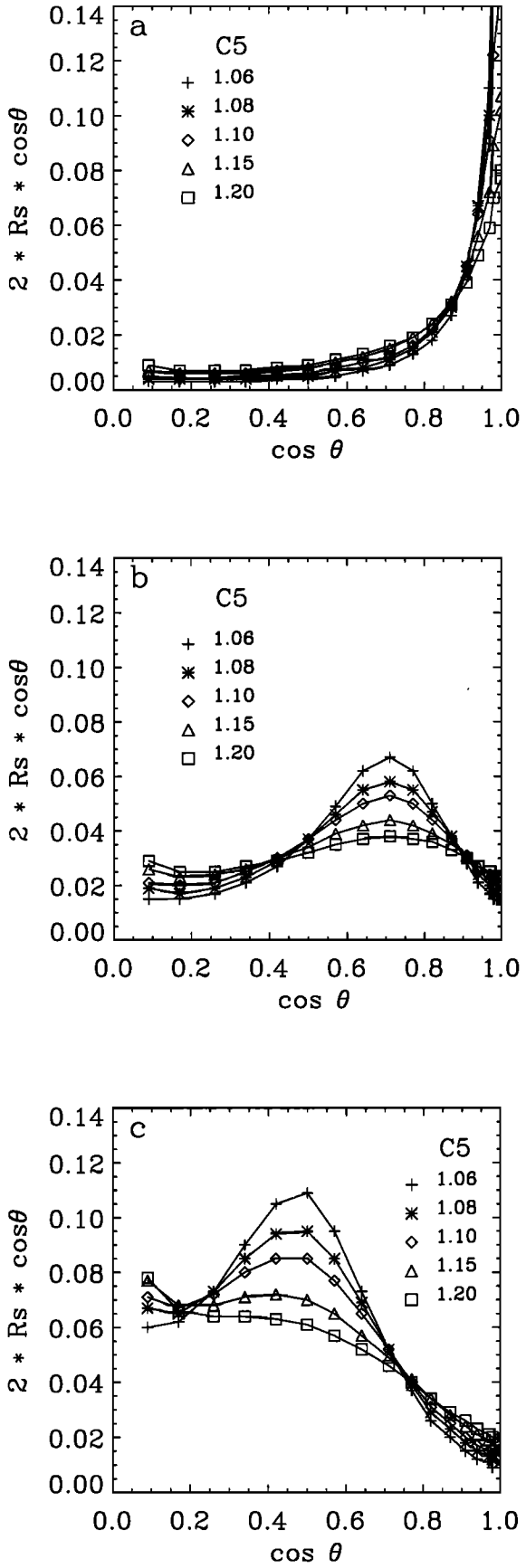

Figure A3. Specular term $2R_s\cos\theta$ vs. $\cos\alpha$ for C_4 = 0.0080. (a) SZA = 0°; (b) = SZA = 45°; (c) SZA = 60°.

Figures A1a - A1c depict A_2 as a function of u for three solar zenith angles, ζ = 0°, 45°, and 60°. These curves are the same for any value of C_4 since A_2 is independent of C_4. The peak in each solar zenith case occurs where $u = u_0$. The smaller the value of C_5 the greater the area under the curve.

The specular model albedo is computed by numerically integrating equation (A2) over the viewing zenith angle as

$$a(\zeta) = 2\int_0^1 R_s u\,du \tag{A6}$$

Figures A2a - A2c and figures A3a - A3c for C_4 = 0.0056 and C_4 = 0.008, respectively, show $2R_s\mu$ as a function of u for varying values of C_5 for the three incident angles. As C_4 increases, the specular term increases. The peak for each case occurs at $u = u_0$. The C_5 is associated with surface roughness in the specular term. An increase in this parameter can be interpreted as an increase in wind speed and a decrease corresponds to low or calm conditions. From these figures, a low C_5 corresponds to high specular peak, while a large C_5 corresponds to a broadening of the specular term.

For each solar zenith angle, albedo is computed from equation (A6). D is computed as

$$D = \frac{1}{N}\Sigma a(\zeta)u_0^2 \tag{A7}$$

where N = 3 (i.e., ζ = 0°, 45°,60°).

Acknowledgments. This research was supported by NASA contract NAS1-19570 with Analytical Services and Materials, Inc., with whom the first author is employed.

References

Barkstrom, B. R., Earth radiation budget measurements: Pre-ERBE, ERBE, and CERES, in *Long-Term Monitoring of the Earth's Radiation Budget*, edited by Bruce R. Barkstrom, *Proc. SPIE 1299*, 52-60, 1990.

Barkstrom, B. R., and G. L. Smith, The Earth Radiation Budget Experiment: Science and implementation, *Rev. Geophys., 24*, 379 - 390, 1986.

Brennan, B., M. Haley, and I. Strange, A Radiation climatology in the visible and infrared from TIROS meteorological satellites, *NASA TN D-2534*, 1965.

Chandrasekhar, S., *Radiative Transfer*, Dover, Mineola, N. Y., 1960.

Coulson, K. L., G. M. Bouricius, and E. L. Gray, Optical reflection properties of natural surfaces, *J. Geophys. Res., 70*, 4601 - 4611, 1965.

Coulson, K. L., and D. W. Reynolds, The spectral reflectance of natural surfaces, *J. Appl. Meteorol., 10*, 1285 -1295, 1971.

Cox, C., and W. Munk, Measurements of the roughness of the sea surface from photographs of the Sun's glitter, *J. Opt. Soc. Am., 44*, 838 - 850,1954.

Dlhopolsky, R., and R. Cess, Improved angular directional models for clear sky ocean derived from the Earth Radiation Budget Satellite shortwave radiances, *J. Geophys. Res., 98*, 16,713 -16,721, 1993.

Green, R. N., and G. L. Smith, Shortwave shape factor inversion of the Earth Radiation Budget observations, *J. Atmos. Sci., 3*, 390 - 402, 1990.

Jacobowitz, H., H. V. Soule, H. L. Kyle, F. B. House, and the Nimbus-7 ERB Experiment Team, The Earth Radiation Budget (ERB) Experiment: An overview, *J. Geophys. Res., 89*, 5021-5038, 1984.

Larsen, J. C., and B. R. Barkstrom, Effects of realistic angular reflection laws for Earth's surface upon calculations of the Earth-atmosphere albedo, paper presented at the Symposium on Radiation in the Atmosphere, Garmisch-Partenkirchen, Germany, 1977.

Manalo, N. D. and G. L. Smith, Scene identification probabilities for evaluating radiation flux errors due to scene misidentification, paper presented at the Seventh Symposium on Meteorological Observations and Instrumentation, Am. Meteorol. Soc., New Orleans, La., 1991.

Raschke, E., T. H. Vonder Haar, W. R. Bandeen, and M. Pasternak, The annual radiation balance of the Earth-atmosphere system during 1969 - 1970 from the Nimbus 3 measurements, *J. Atmos. Sci., 30*, 341 - 364, 1973.

Ruff, I., R. Koffler, S. Fritz, J. S. Winston, and P. K. Rao, Angular distribution of solar radiation reflected from clouds as determined from TIROS IV radiometer measurements, *J. Atmos. Sci., 25*, 323 - 332, 1968.

Salomonson, V., and W. E. Marlatt, Anisotropic solar reflectance over white sand, snow and stratus clouds, *J. Appl. Meteor., 7*, 475 - 483, 1968.

Smith, G. L., R. N. Green, E. Raschke, L. M. Avis, J. T. Suttles, B. A. Wielicki, and R. Davies, Inversion methods for satellite studies of the Earth's radiation budget: Development of algorithms for the ERBE Mission, *Rev. Geophys., 24*, 407 - 421, 1986.

Smith, G. L., J. T. Suttles, and N. D. Manalo, The ERBE Alongtrack Scan Experiment, *Proc. International Radiation Symp*, 242 - 244, Lille, France, 1988.

Smith, W. L., J. Hickey, H. B. Howell, H. B. Jacobowitz, D. T. Hilleary, and A. J. Drummond, Nimbus-6 Earth Radiation Budget Experiment, *Appl. Opt., 16*, 306 - 318, 1977.

Staylor, W. F., Reflection and emission models for clouds derived from Nimbus 7 Earth Radiation Budget scanner measurements, *J. Geophys. Res, 90*, 8075 - 8079, 1985.

Staylor, W. F., Site selection and directional models of deserts used for ERBE validation targets, *NASA Tech. Pap. 2540*, 1986.

Staylor, W. F., and J. T. Suttles, Reflection and emission models for deserts derived from Nimbus 7 ERB scanner measurements, *J. Clim. Appl. Meteorol.*, 25, 196 - 202, 1986.

Suttles, J. T., R. N. Green, P. Minnis, G. L. Smith, W. F. Staylor, B. A. Wielicki, I. J. Walker D. F. Young, V. R. Taylor, and L. L. Stowe, *Angular* Radiation Models for Earth-Atmosphere System, vol. 1, NASA Ref. Publ. 1184, 1988.

Suttles, J. T., B. A. Wielicki, and S. Vemury, Top of atmosphere radiative fluxes: Validation of ERBE scanner inversion algorithm using Nimbus 7 ERB data, *J. Appl. Meteorol., 31*, 784 - 796, 1992.

Taylor, V. R., and L. L. Stowe, Reflectance characteristics of uniform Earth and cloud surfaces derived from NIMBUS 7 ERB, *J. Geophys. Res., 89*, 4987 - 4996, 1984.

Wielicki, B. A., and R. N. Green, Cloud identification for ERBE radiative flux retrieval, *J. Appl. Meteorol., 28*, 1133 -1146, 1989.

N. Manalo-Smith, Analytical Services and Materials, Inc., 1 Enterprise Parkway, Suite 300, Hampton, VA 23666. (e-mail: n.m.smith@larc.nasa.gov).

G. L. Smith, Virginia Polytechnic Institute and State University, Hampton, VA 23681. (e-mail: g.l.smith@larc.nasa.gov).

S. N. Tiwari, Department of Mechanical Engineering, Old Dominion University, 238 Kaufman Hall, Norfolk, VA 23529. (e-mail: june@mem.odu.edu).

W. F. Staylor, Formerly at Atmospheric Sciences Division, Langley Research Center, NASA, Hampton, VA 23681.

(Received January 24, 1997; revised July 1, 1997;
accepted January 8, 1998.)